NANO LETTERS

pubs.acs.org/NanoLett

Letter

Electric Fields and Charge Separation for Solid Oxide Fuel Cell Electrodes

Nicholas J. Williams,* Ieuan D. Seymour, Dimitrios Fraggedakis, and Stephen J. Skinner

Cite This: *Nano Lett.* 2022, 22, 7515−7521

Read Online

ACCESS | Metrics & More | Article Recommendations | Supporting Information

ABSTRACT: Activation losses at solid oxide fuel cell (SOFC) electrodes have been widely attributed to charge transfer at the electrode surface. The electrostatic nature of electrode−gas interactions allows us to study these phenomena by simulating an electric field across the electrode−gas interface, where we are able to describe the activation overpotential using density functional theory (DFT). The electrostatic responses to the electric field are used to approximate the behavior of an electrode under electrical bias and have found a correlation with experimental data for three different reduction reactions at mixed ionic−electronic conducting (MIEC) electrode surfaces (H_2O and CO_2 on CeO_2; O_2 on $LaFeO_3$). In this work, we demonstrate the importance of decoupled ion−electron transfer and charged adsorbates on the performance of electrodes under nonequilibrium conditions. Finally, our findings on MIEC−gas interactions have potential implications in the fields of energy storage and catalysis.

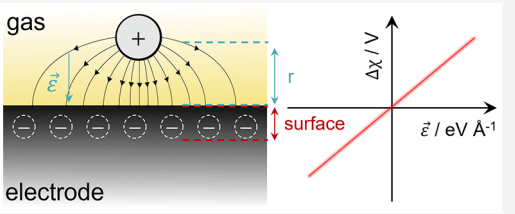

KEYWORDS: *DFT, SOFC, electric field, surface potential, thermodynamics*

Downloaded via UNIV OF ABERDEEN on June 13, 2023 at 10:38:37 (UTC).
See https://pubs.acs.org/sharingguidelines for options on how to legitimately share published articles.

Electrochemical devices, such as solid-oxide fuel cells (SOFCs), allow for reversible chemical to electrical energy conversion, with efficiency surpassing that of the combustion engine.[1] The Faradaic reactions at the fuel (i.e., $H_{2(g)}$ or $CO_{(g)}$) and air electrodes of an SOFC can be given simply as[2,3]

$$\text{fuel electrode: } H_{2(g)} + O^{2-} \rightarrow H_2O_{(g)} + 2e^- \quad (1)$$

$$\text{air electrode: } \frac{1}{2}O_{2(g)} + 2e^- \rightarrow O^{2-} \quad (2)$$

where O^{2-} and e^- represent oxide ions in the electrolyte and electrons in the electrode, respectively. The dipole at the electrode−liquid electrolyte interface, known as the activation overpotential (η_{act}), accounts for the energy barrier of charge-transfer processes such as Li-ion intercalation.[4−8] For SOFC systems, these phenomena do not apply, and little is known about the electrode−gas interactions that determine the activation overpotential. The ambipolar transfer of ions and electrons with the gas phase means that this interface is chemical in nature.[9] However, in the limit where one of these charge-transfer processes is particularly slow, the adsorbed gas will become charged and will therefore impose an electrostatic surface potential (χ) across the electrode−gas interface.

The process of gas reduction at a MIEC surface can be generalized as[10,11]

$$Ox_{(g)} + V_{ode}^{n+} + ne_{ode}^- \rightleftharpoons Red_{ode} \quad (3)$$

where $Ox_{(g)}$, V_{ode}^{n+}, e_{ode}^- and Red_{ode} represent the oxidized gas species (i.e., $O_{2(g)}$ or $H_2O_{(g)}$), the vacant surface site, mobile electrons, and the reduced species, respectively. Superscript n represents the charge of the vacant site and the number of electrons consumed by an ambipolar charge-transfer reaction. In the theory outlined by Fraggedakis et al., Faradaic reactions at an electrode−electrolyte interface can proceed through a coupled ion−electron transfer (CIET) mechanism.[4] The excess chemical potential landscape in Figure 1a−c illustrates three scenarios of ion−electron transfer. When the barrier for ion transfer (IT) is significantly lower than that for the possible electron-transfer (ET) step (Figure 1a), the charge-transfer process is decoupled. As such, the adsorbate will hold the charge of the vacancy which it filled and will develope an electrostatic surface potential. In the second case (Figure 1b), both IT and ET can occur simultaneously through a concerted mechanism. In such a situation, there is no stable intermediate state and no charged adsorbate exists on the electrode surface. Therefore, charge separation does not occur, and no electrostatic surface potential is observed. Last, when the energy barrier for IT is significantly larger than ET, the gas species will be reduced before the rate-limiting IT step (Figure 1c). Similar to the ET-limited case, the charge-transfer process is decoupled and the adsorbate will hold a charge equal to the

Received: June 22, 2022
Revised: August 24, 2022
Published: September 6, 2022

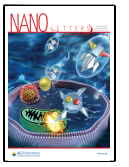

ACS Publications

© 2022 The Authors. Published by American Chemical Society

https://doi.org/10.1021/acs.nanolett.2c02468
Nano Lett. 2022, 22, 7515−7521

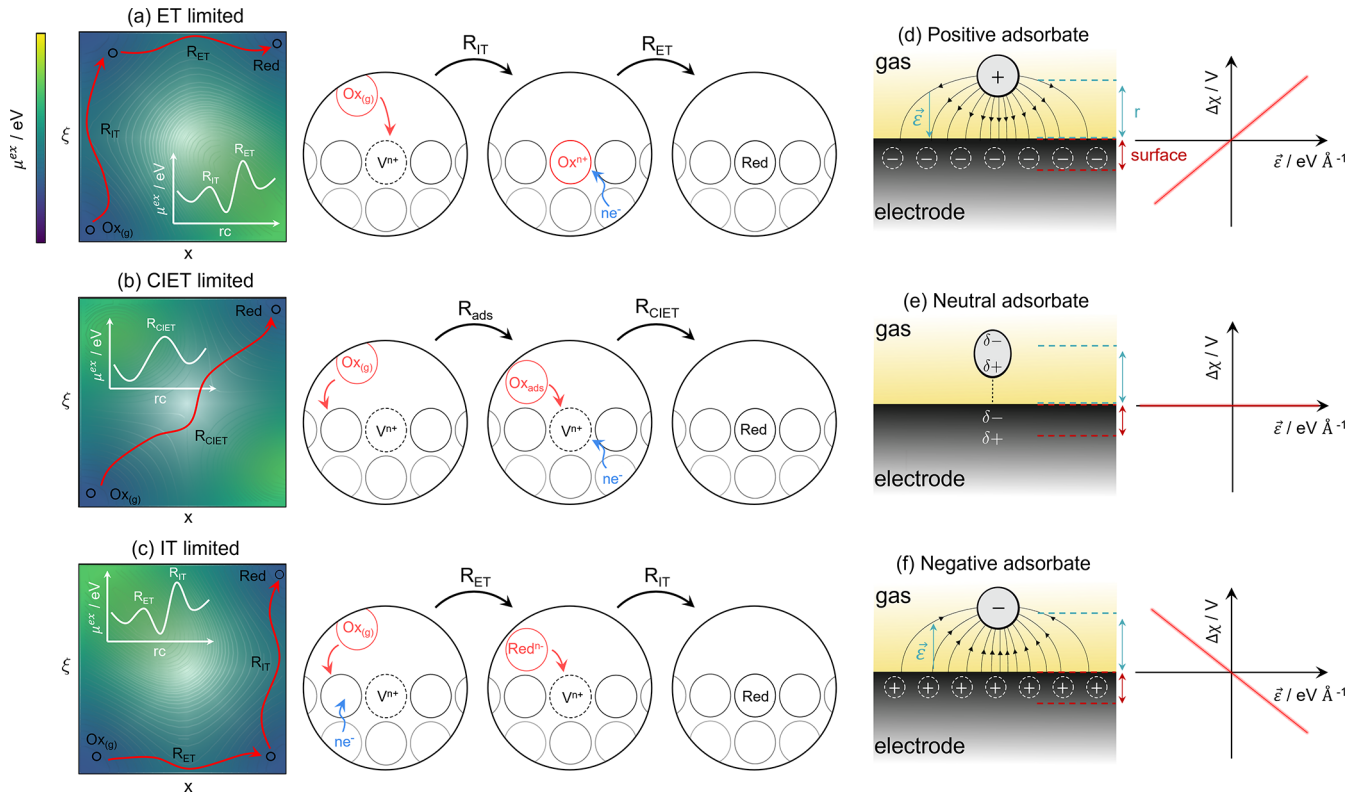

Figure 1. Left-hand column details the excess chemical potential energy landscape for (a) ET limited reduction, (b) CIET limited reduction, and (c) IT limited reduction. The planes represent the ET reaction coordinates (x) and the IT reaction coordinate (ξ).[4] The white plots represent the 1D chemical potential landscape explored by the reduction reaction. R_{ads} is the adsorption step, R_{ET} is the electron-transfer (ET) step, R_{IT} is the IT step, and R_{CIET} is the CIET step. The right-hand column details a schematic illustration of the shift in electric potential of an electrode experiencing a negative overpotential, where the black and red lines represent the potential at the point of zero charge (PZC) and under a negative applied electric field, respectively. (d) Positive adsorbate induces an electric field vector pointing into the electrode surface, where $\Delta\chi - \eta_{act}$ has a positive correlation, (e) a neutral adsorbate induces no electric field with no correlation, and (f) a negative adsorbate induces an electric field vector pointing away from the electrode surface, yielding a negative $\Delta\chi - \eta_{act}$ correlation.

number of electrons transferred in the ET step, resulting in an electrostatic surface potential.

In a previous study, we determined that the electrostatic surface potential had a profound influence on the gas reduction kinetics, where a $\Delta\chi \neq 0$ relationship is desirable.[12,13] Few experiments have investigated the complex $\Delta\chi - \eta_{act}$ relationship, leaving this phenomenon poorly understood despite its kinetic merit.[12,14−17] By analyzing the shift in the outer work function using *operando* X-ray photoelectron spectroscopy (XPS) over an applied overpotential range, Feng et al. measured the $\Delta\chi - \eta_{act}$ relationship for three different electroreduction systems illustrated in Figure 2. Mechanistic details given in Table 1 and Table S1 show the overpotential derived from each reaction. Upon expanding the electrochemical potential terms, we find the general solution $ne\eta_{act} = \pm T\Delta S \pm ne\Delta\chi$. Thus, each derivation finds a relationship consistent with which electrons and adsorbates interact.[9,18] They also concluded that the space−charge potential at the electrode surface was invariant under an applied overpotential (i.e., H_2O and CO_2 on CeO_2; O_2 on $LaFeO_3$).[9] While this finding points toward the existence of an active mechanism controlling the electrochemical performance of electrified interfaces, the theoretical understanding is still in its early stages. Here, we rationalize the mechanistic basis of these observations.

As defined by Bazant, the internal energy, or open circuit voltage (V_0), of a uniform reactive mixture is given as the first variational derivative of the Gibbs free energy (G) with respect to the concentration[8]

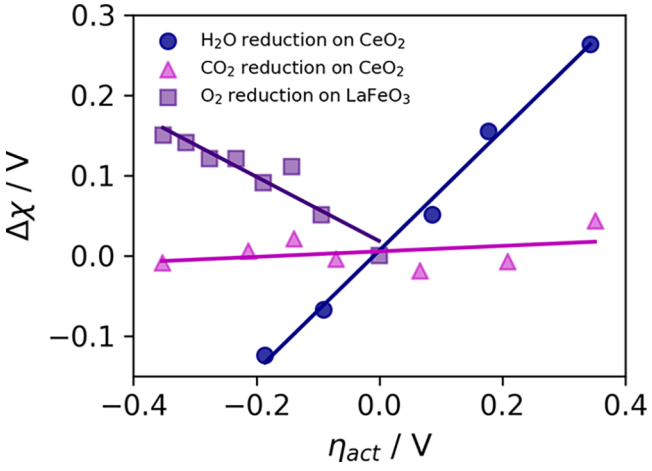

Figure 2. Experimental shift in the electrostatic surface potential as a function of the overpotential relationship at the $Sm_{0.2}Ce_{0.8}O_{1.9}$−gas interface in 0.35 mbar 1:8:4 $H_2/H_2O/Ar$ (blue circles), 0.36 mbar 2:25 CO/CO_2 (magenta triangles), and $La_{0.8}Sr_{0.2}FeO_3$ in 1.3 mbar O_2 (purple squares).[9,18] The solid line represents the linear fit to the experimental data with gradients $\partial\Delta\chi/\partial\eta_{act}$ = 0.75, 0.03, and −0.40 for H_2O reduction, CO_2 reduction, and O_2 reduction, respectively.

https://doi.org/10.1021/acs.nanolett.2c02468
Nano Lett. 2022, 22, 7515−7521

Table 1. Steps in Gas Reduction at the MIEC Surface for Three Systems Investigated Experimentally, Written in Kröger–Vink Notation, Where the Reported Rate-Limiting Step for Each Process Is Given in Bold[9,15,19−21a]

H_2O reduction on CeO_2	
$H_2O_{(g)} + V_O^{\bullet\bullet} + O_O^x \rightleftharpoons 2OH_O^{\bullet}$	$2e\eta_{act} = -T\Delta S_{conf} - 2e\Delta\chi$
$\mathbf{2OH_O^{\bullet} + 2Ce'_{Ce} \rightleftharpoons H_{2(g)} + 2O_O^x + 2Ce_{Ce}^x}$	$2e\eta_{act} = -T\Delta S_{conf} + 2e\Delta\chi$
CO_2 reduction on CeO_2	
$CO_{2(g)} + O_O^x \rightleftharpoons CO_{3O}^x$	$2e\eta_{act} = -T\Delta S_{conf}$
$\mathbf{CO_{3_O}^x + 2Ce'_{Ce} + V_O^{\bullet\bullet} \rightleftharpoons CO_{(g)} + 2O_O^x + 2Ce_{Ce}^x}$	$2e\eta_{act} = -T\Delta S_{conf}$
O_2 reduction on $LaFeO_3$	
$^1/_2O_{2(g)} + Fe_{Fe}^x \rightleftharpoons O'_{ads} + Fe_{Fe}^{\bullet}$	$e\eta_{act} = T\Delta S_{conf} + e\Delta\chi$
$O'_{ads} + V_O^{\bullet\bullet} + Fe_{Fe}^x \rightleftharpoons O_O^x + Fe_{Fe}^{\bullet}$	$e\eta_{act} = T\Delta S_{conf} - e\Delta\chi$

[a]For H_2O reduction, steam adsorption is an IT step which consumes an oxygen vacancy ($V_O^{\bullet\bullet}$) and forms two hydroxyls ($OH_O^{\bullet}$) on the surface. This is followed by the rate-limiting ET step which consumes two polarons (Ce'_{Ce}) and forms $H_{2(g)}$. For CO_2 reduction, the first step forms an adsorbed neutral carbonate (CO_{3O}^x) which then undergoes the rate-limiting CIET step to form $CO_{(g)}$. For O_2 reduction, we assume fast dissociate adsorption and ET forming a negatively charged adsorbate (O'_{ads}) and a polaronic hole ($Fe_{Fe}^{\bullet}$). The second step is the rate-determining incorporation step which includes a single electron transfer and consumes an oxygen vacancy.[15] The activation overpotential equations are given for each reaction step derived in Table S1, where ΔS_{conf} is the change in configurational entropy under nonequilibrium.

$$\mu_h = \frac{\delta G}{\delta c} = \mu^{\Theta} + \frac{dg_h}{dc} \tag{4}$$

where μ^{Θ} and g_h represents the standard chemical potential and homogeneous free energy density of the mixture, respectively. The reservoir chemical potential (μ_{res}), or cell voltage (V), acts as the nonequilibrium chemical potential of the system.[22] The difference between the internally controlled potential (μ_h) and the externally controlled potential (μ_{res}) is given by the reaction affinity, $A = \mu_{res} - \mu_h$, which controls the rate of a reduction reaction.[22] This can also be expressed as the activation overpotential[4,7,8]

$$ne\eta_{act} = \mu_{res} - \mu_h \tag{5}$$

where n is the number of electrons transferred in the Faradaic reaction. The Fermi energy (E_F) describes the electrochemical potential of free electrons, and the shift in the Fermi energy describes the activation overpotential at each electrode (illustrated in Figure S1)[9,19]

$$\eta_{act,fuel} = \mu_{e^-} = \Delta E_{F,fuel} \tag{6}$$

$$\eta_{act,air} = -\mu_{e^-} = -\Delta E_{F,air} \tag{7}$$

where under a positive overpotential (fuel cell mode) gas is oxidized by the fuel electrode and reduced by the air electrode (full derivation in SI). The formation of the electrostatic surface potential can be described as the difference in electrostatic potential of free electrons in the electrode (ϕ_e) and the adsorbate (ϕ_{ad}):[12,16]

$$\chi = \phi_e - \phi_{ad} \tag{8}$$

Under bias, an electrostatic potential shift is defined at the surface as

$$\Delta\chi = \chi - \chi^{eq} \tag{9}$$

where an effective electrical double layer is formed between the electrode surface and the adsorbed species.

The interface between the adsorbate and the electrode can be understood as a parallel plate capacitor where the electric field ($\vec{E}$) is controlled by the voltage (V) and the distance (r) between the adsorbed species and the first layer of the surface, $\vec{E} = V/r$. However, modulating the adsorbate–electrode distance will result in an energetically unfavorable distortion of the bonding. Therefore the shift in the electrostatic surface potential is a result of a change in the coverage of polar adsorbates such that $\chi = (\vec{\mu}_\perp \rho_0 \theta)/\epsilon_0$ where $\vec{\mu}_\perp$, ε_0, ρ_0, and θ represent the dipole moment normal to the surface, vacuum permittivity, density of available adsorption sites, and adsorbate coverage, respectively.[16] A positively charged adsorbate (Figure 1d) imposes a negative electric field vector which points into the electrode surface ($\vec{\mathcal{E}} = -\nabla\phi$). A neutral adsorbate (Figure 1e) has no electrostatic attraction to the electrode and is therefore weakly bound to the oxide surface by dipolar interactions. Finally, a negatively charged adsorbate (Figure 1f) imposes a positive electric field which points away from the electrode surface.

Advances in the modeling of electrochemical interfaces have allowed computational chemists to study charged surfaces by incorporating electric fields into electronic structure simulations using density functional theory (DFT) as illustrated in Figure S3.[5,23] For electrochemical processes which induce the polarization of electron density, the corresponding reaction energy depends on the electrochemical potential of the surface, where the effects of the electric field are found to be strongly dependent on its dipole moment and polarizability, according to[5,23,24]

$$U_i(\vec{\mathcal{E}}) = U_i^{PZC} + \vec{\mu}_\perp \vec{\mathcal{E}} - \frac{\alpha}{2}\vec{\mathcal{E}}^2 \tag{10}$$

where U_i^{PZC} is the internal energy at the point of zero charge and α is the polarizability. Equation 10 implies that a surface with a positive dipole moment is stabilized by a negative electric field vector and vice versa. As such, the electrostatic surface potential can be described by the difference in dipole moment between the products and reactants, $\Delta\vec{\mu}_\perp = \vec{\mu}_{\perp,p} - \vec{\mu}_{\perp,r}$,

$$ne\Delta\chi(\vec{\mathcal{E}}) = \Delta U_{rxn}(\vec{\mathcal{E}}) - \Delta U_{rxn}^{PZC} = \Delta\vec{\mu}_\perp \cdot \vec{\mathcal{E}} = \left(\frac{\partial \Delta U_{rxn}(\vec{\mathcal{E}})}{\partial \vec{\mathcal{E}}}\right)\cdot\vec{\mathcal{E}} \tag{11}$$

where $\Delta U_{rxn} = U_p - U_r$ is the change in internal energy of the reduction reaction. The electrostatic potential experienced by mobile charges in the MIEC electrode phase will shift in accordance with the activation overpotential, as described by eqs 6 and 7.[25] This is analogous to applying an electric field, where the Fermi energy response can be used to determine the activation overpotential:[19,24]

$$\eta_{act,fuel}(\vec{\mathcal{E}}) = \left(\frac{\partial E_{F,fuel}(\vec{\mathcal{E}})}{\partial \vec{\mathcal{E}}}\right)\cdot\vec{\mathcal{E}} \tag{12}$$

$$\eta_{act,air}(\vec{\mathcal{E}}) = -\left(\frac{\partial E_{F,air}(\vec{\mathcal{E}})}{\partial \vec{\mathcal{E}}}\right)\cdot\vec{\mathcal{E}} \tag{13}$$

It is therefore possible to predict the origin of the activation overpotential for adsorbed gas species by combining eq 11

https://doi.org/10.1021/acs.nanolett.2c02468
Nano Lett. 2022, 22, 7515−7521

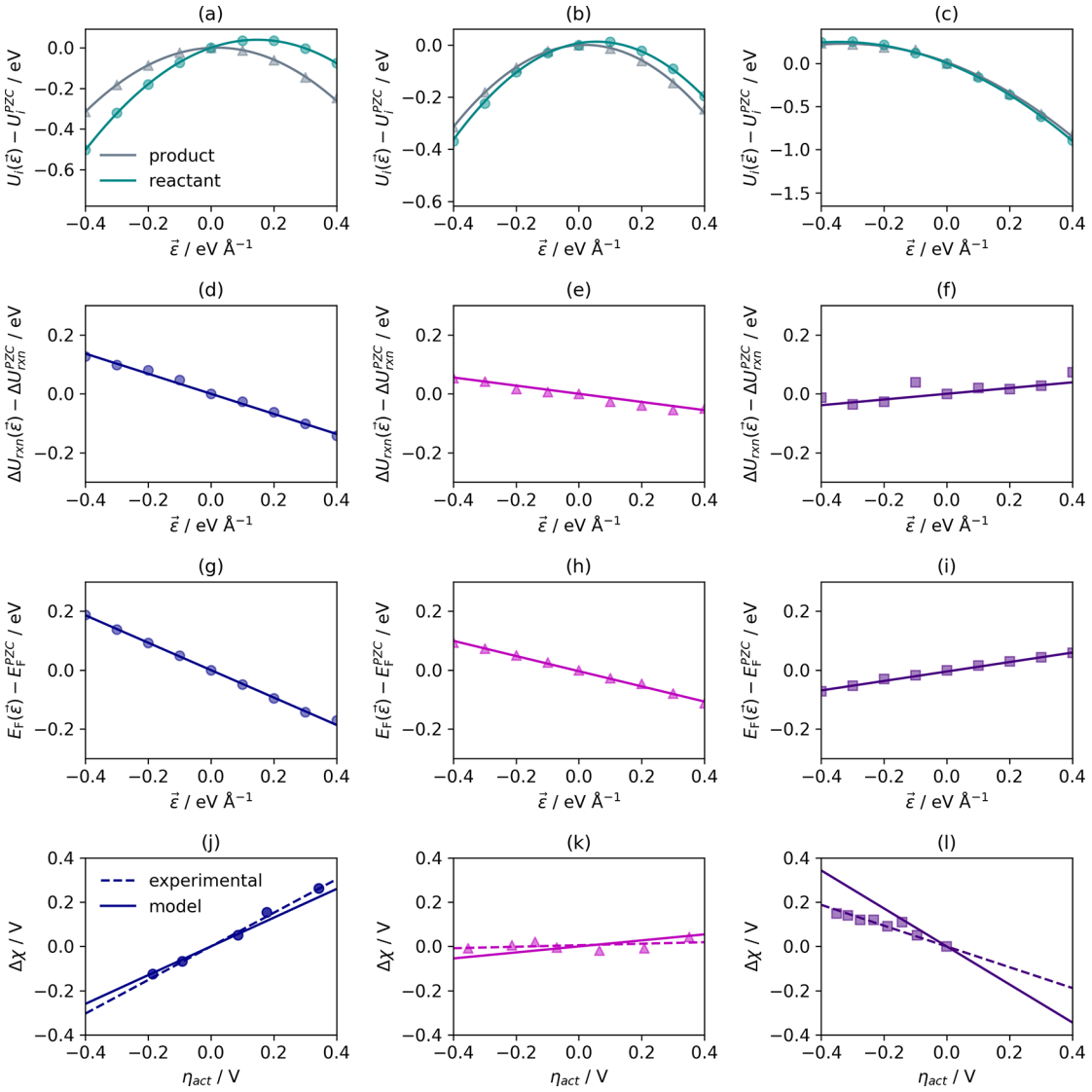

Figure 3. (a–c) Internal energy calculation as a function of the applied electric field fit to eq 10, (d–f) internal energy of the reaction response to an applied electric field where solid lines represent the fit to eq 11, (g–i) Fermi energy response to an applied electric field, where solid line represents the fit to eq 12 and 13, and experimental shift in the electrostatic surface potential as a function of the overpotential relationship at the $Sm_{0.2}Ce_{0.8}O_{1.9}$–gas interface in (j) 0.35 mbar 1:8:4 $H_2/H_2O/Ar$ (blue circles),[9] (k) 0.36 mbar 2:25 CO/CO_2 (magenta triangles),[9] and (l) $La_{0.8}Sr_{0.2}FeO_3$ in 1.3 mbar O_2 (purple squares).[18] The dashed and solid lines represent the linear fit to the experimental data and simulated results, respectively.

with eq 12 or 13.[5] In this work, using a novel computational framework, we are able to predict the $\eta_{act} - \Delta\chi$ relationship of an electrode–adsorbate system using applied electric fields.

DFT calculations were carried out to determine the internal energy (U) of the reactant and product configurations of the rate-limiting step for the reduction reactions detailed in Table 1 as a function of the applied electric fields (Figure 3a–c). By taking the energy difference between the reactants and products, the reduction driving force (eq 11) is given as a function of electric field (Figure 3d–f). We then determined the shift in Fermi energy of the surface with free charges (Ce'_{Ce} or $Fe^{\bullet}_{Fe}$) as a function of the appled electric field (Figure 3g–i). The simulated $\Delta\chi - \eta_{act}$ relationship for the three systems (Figure 3j–l) considered is given in Table S2.

For H_2O reduction on CeO_2, the gradient $\partial\Delta\chi(\vec{\mathcal{E}})/\partial\eta_{act}(\vec{\mathcal{E}}) = 0.65$ is in good agreement with the linear fit to the experimental data $\partial\Delta\chi/\partial\eta_{act} = 0.76$ (Figure 3j). The error can be attributed to lateral interactions between dipoles which occur when the adsorbate coverage is greater than approximately 1%, where the intrinsic dipole moment imposed by the adsorbate is dependent on the coverage.[12,16] DFT calculations were carried out at $\theta_{OH_O} = 0.125$, which is close to the experimentally measured coverage at PZC and is where the model and data best agree. However, as η_{act} is increased, the model and experimental results deviate as the hydroxyl coverage decreases, increasing the strength of the intrinsic dipole moment and increasing the gradient $\partial\Delta\chi/\partial\eta_{act}$. Mechanistically, the ambipolar charge-transfer reaction is decoupled, where the fast adsorption step (Table 1) fills a charged oxygen vacancy (IT) and the ET step becomes rate-limiting. Table 1 illustrates the $\Delta\chi - \eta_{act}$ relationships derived from each reaction step, where we have shown that ET is rate-limiting to derive the experimental trend $\Delta\chi \approx \eta_{act}$.

https://doi.org/10.1021/acs.nanolett.2c02468
Nano Lett. 2022, 22, 7515–7521

For CO_2 reduction on CeO_2, the gradient $\partial\Delta\chi(\vec{\mathcal{E}})/\partial\eta_{act}(\vec{\mathcal{E}}) = 0.13$ also agrees with the linear fit to the experimental data $\partial\Delta\chi/\partial\eta_{act} = 0.03$ (Figure 3k). The true CeO_2 surface will have many arrangements of the electronic defects, causing the net electrostatic potential to cancel. Here we have analyzed only one such defect complex which has a relatively small dipole moment ($\vec{\mu}_\perp = 0.14e$), accounting for the model's overestimation of the electrostatic surface potential. With respect to the surface chemistry, the ambipolar charge-transfer reaction remains coupled. As such, there is no stable charged adsorbate state, so a negligible electrostatic surface potential is observed.

Contrary to previous suggestions regarding the magnitude of the electrostatic surface potential, fast kinetics are not entirely based upon the strength of the intrinsic dipole moment of the adsorbate.[15,16] As we observed for CO_2 reduction on CeO_2, the intrinsic dipole moment of the carbonate is relatively large ($\vec{\mu}_\perp = 1.09e$), yet the shift in electrostatic surface potential is zero. This results from the neutrality of the adsorbate ($CO^x_{3_O}$) and the absence of charge separation, meaning that the carbonate will experience a change in the chemical potential only under an applied overpotential (Table 1).[9]

For O_2 reduction on $LaFeO_3$, the gradient $\partial\Delta\chi(\vec{\mathcal{E}})/\partial\eta_{act}(\vec{\mathcal{E}}) = -0.86$ while the linear fit to the experimental data $\partial\Delta\chi/\partial\eta_{act} = -0.47$ (Figure 3l).[18] The general trend is captured correctly; however, the model overestimates the shift in the electrostatic surface potential. The most obvious reason for the error observed in Figure 3l is the simplicity of the model, where strontium was not included in the DFT calculation. We chose to use Fe on the surface layer because it was reported to be the most stable termination under operational conditions.[26] However, we found that using strontium or lanthanum in the terminating layer had a negligible effect on the dipole moment of the surface. Additionally, doping strontium into the subsurface layer also had a negligible effect on the dipole moment of the surface. Guan found inconsistencies in the $\partial\Delta\chi/\partial\eta_{act}$ relationship with respect to variations in the La/Sr ratios.[18] Guan also observed that the $\partial\Delta\chi/\partial\eta_{act}$ relationship was dependent on the p_{O_2} value of the environment. This suggests that the shift in surface potential was limited by the equilibrium potential. Fleig proposed that the buffering effect was due to the limited coverage of adsorbed gas on the surface at the PZC.[27]

With respect to the mechanism for charge transfer, the ambipolar charge-transfer reaction has been decoupled by slow IT. This agrees with the derivation in Table 1, where the IT step yields the experimentally given relationship $\Delta\chi \approx -\eta_{act}$. While we strongly believe that the results of this study show that O_2 reduction on MIEC surfaces is driven by $\Delta\chi$, we must also note that the exact mechanism is subject to discord. Therefore, we do not intend to speculate further on the mechanistic details in this study.

We have described the effect of electric fields on the electrostatic surface potential at the MIEC−gas interface. By integrating an electric field with first-principles calculations, we validated the model to correctly predict the nature of the electrostatic surface potential for three experimentally studied systems. Furthermore, we have determined a link between the electrostatic surface potential and the mechanistic nature of the rate-limiting charge-transfer reaction, where we illustrated the importance of decoupled charge transfer for optimum kinetics. These kinetic effects may also be applied to other MIEC systems for energy storage and conversion.

CALCULATION METHODS

Spin-polarized density functional theory (DFT) calculations were carried out using the Vienna *Ab initio* Simulation (VASP) code.[28] The ionic cores were described by PAW potentials (an O pseudopotential was used for oxygen), and the wave functions were expanded in plane waves with an energy cutoff at 520 eV.[29] The PBE-generalized gradient approximation (GGA) was used.[30,31] To describe the Ce 4f and Fe 3d electrons, DFT+U was implemented using the Dudarev treatment.[31−33] For Ce 4f electrons, we used $U_{eff} = 5$ eV following the work of Castleton et al., and for the Fe 3d electrons, we used $U_{eff} = 3$ eV following the work of Grau-Crespo et al.[34,35] The surfaces were modeled as symmetric slabs with a thickness of 12 atomic layers and 3 × 3 cell expansion in the lateral directions. The bottom three atomic layers were fixed during geometry optimizations. The periodic images of the slab were separated along the *c* direction by a vacuum region of about 15 Å. The convergence parameters for electronic and ionic relaxation were set to 10^{-7} and 10^{-4} eV, respectively, to guarantee the sufficient accuracy of the calculated forces. The dipole correction was used to decouple the electrostatic interaction between the periodic images. The calculations were performed with a 4 × 4 × 1 Monkhorst Pack grid. For gases, electronic calculations were carried out in a 13 × 14 × 15 $Å^3$ box. The standard chemical potential was calculated as $\mu^\circ = E^{el} + ZPE - TS$, where the entropy of the gas and surface was calculated using the ASE thermochemistry package.[36] Electric fields were implemented using the EFIELD tag.[37]

H_2O Reduction on CeO_2. The $CeO_2(111)$ termination was studied because it was previously reported to be the most stable termination under solid oxide cell operational conditions.[38] Additionally, Feng et al. speculated that the SDC thin film grown on the current collector was (111)-oriented.[39] The rate-limiting step of H_2O reduction on CeO_2 was reported to be ET (Table 1), where we calculate the free energy of the pristine slab and a slab with a singly charged $OH^\bullet_O$ adsorbate (Figure S2a,b).[20]

CO_2 Reduction on CeO_2. Studies on the $CeO_2(110)$ termination reported that the singly charged $CO^\bullet_{3_O}$ state was stable during the reduction of CO_2.[21,40] However, no stable intermediate states were found when exploring the reduction of CO_2 on the $CeO_2(111)$ termination. The rate-limiting step was determined to be CIET, where we calculated the free energy of the pristine slab and a neutral $CO^x_{3_O}$ state on a reduced $CeO_2(111)$ slab (Figure S2c,d).

O_2 Reduction on $LaFeO_3$. The $LaFeO_3(100)$ termination with Fe on the surface layer was reported to be the most stable termination under operational conditions.[26] The IT was reported to be the rate-limiting step (Table 1),[15] where we calculated the free energy of the pristine slab and a charged $O^\bullet_O$ state in which the polaronic hole was located at $Fe^\bullet_{Fe}$ (Figure S2e,f).

ASSOCIATED CONTENT

Supporting Information

The Supporting Information is available free of charge at https://pubs.acs.org/doi/10.1021/acs.nanolett.2c02468.

https://doi.org/10.1021/acs.nanolett.2c02468
Nano Lett. 2022, 22, 7515−7521

Schematic of the potential across the fuel cell at open circuit voltage (V_{cell}), in fuel-cell mode (V_{FC}), and in electrolysis mode (V_{EC}); schematic of the adsorbate state for $2OH^{\bullet}_{O}$ on CeO_2, CO_{3O}^{x} on CeO_2, and O'_O on $LaFeO_3$; derivations of the activation overpotential; schematic illustration of the potential with no applied field and an applied field; Fermi energy, internal energy, and electrostatic surface potential of the reaction as a function of the electric field vector; and derivation of eqs 6 and 7 (PDF)

AUTHOR INFORMATION

Corresponding Author

Nicholas J. Williams − *Department of Materials, Imperial College London, London SW7 2AZ, U.K.; Department of Chemical Engineering, Massachusetts Institute of Technology, Cambridge, Massachusetts 02139, United States*; Email: nw7g140@gmail.com

Authors

Ieuan D. Seymour − *Department of Materials, Imperial College London, London SW7 2AZ, U.K.*

Dimitrios Fraggedakis − *Department of Chemical and Biomolecular Engineering, University of California, Berkeley, California 94720, United States*

Stephen J. Skinner − *Department of Materials, Imperial College London, London SW7 2AZ, U.K.*; orcid.org/0000-0001-5446-2647

Complete contact information is available at: https://pubs.acs.org/10.1021/acs.nanolett.2c02468

Notes

The authors declare no competing financial interest.

ACKNOWLEDGMENTS

This work was supported by Ceres Power Ltd. I.D.S. and S.J.S. acknowledge the EPSRC for funding through the award of grant EP/R002010/1. D.F. (dfrag) acknowledges support from the Miller Institute for Basic Research in Science at the University of California, Berkeley. The authors thank Professor Jan Rossmeisl for fruitful discussions of this work throughout the project.

REFERENCES

(1) Wang, H.; Liu, Y.; Li, M.; Huang, H.; Xu, H. M.; Hong, R. J.; Shen, H. Multifunctional TiO2 nanowires-modified nanoparticles bilayer film for 3D dye-sensitized solar cells. *Optoelectronics and Advanced Materials, Rapid Communications* **2010**, *4*, 1166−1169.

(2) Guan, Z.; Chen, D.; Chueh, W. C. Analyzing the dependence of oxygen incorporation current density on overpotential and oxygen partial pressure in mixed conducting oxide electrodes. *Phys. Chem. Chem. Phys.* **2017**, *19*, 23414−23424.

(3) Dierickx, S.; Weber, A.; Ivers-Tiffée, E. How the distribution of relaxation times enhances complex equivalent circuit models for fuel cells. *Electrochim. Acta* **2020**, *355*, 136764.

(4) Fraggedakis, D.; McEldrew, M.; Smith, R. B.; Krishnan, Y.; Zhang, Y.; Bai, P.; Chueh, W. C.; Shao-Horn, Y.; Bazant, M. Z. Theory of coupled ion-electron transfer kinetics. *Electrochim. Acta* **2021**, *367*, 137432.

(5) Kelly, S. R.; Kirk, C.; Chan, K.; Nørskov, J. K. Electric field effects in oxygen reduction kinetics: rationalizing Ph dependence at the Pt(111), Au(111), and Au(100) electrodes. *J. Phys. Chem. C* **2020**, *124*, 14581−14591.

(6) Lai, W.; Ciucci, F. Mathematical modeling of porous battery electrodes-Revisit of Newman's model. *Electrochim. Acta* **2011**, *56*, 4369−4377.

(7) Bazant, M. Z. Theory of chemical kinetics and charge transfer based on nonequilibrium thermodynamics. *Acc. Chem. Res.* **2013**, *46*, 1144−1160.

(8) Bazant, M. Z. Thermodynamic stability of driven open systems and control of phase separation by electro-autocatalysis. *Faraday Discuss.* **2017**, *199*, 423−463.

(9) Feng, Z. A.; Balaji Gopal, C.; Ye, X.; Guan, Z.; Jeong, B.; Crumlin, E.; Chueh, W. C. Origin of overpotential-dependent surface dipole at CeO_{2-x}/gas interface during electrochemical oxygen insertion reactions. *Chem. Mater.* **2016**, *28*, 6233−6242.

(10) Holzer, L.; Iwanschitz, B.; Hocker, T.; Munch, B.; Prestat, M.; Wiedenmann, D.; Vogt, U.; Holtappels, P.; Sfeir, J.; Mai, A.; Graule, T. Microstructure degradation of cermet anodes for solid oxide fuel cells: Quantification of nickel grain growth in dry and in humid atmospheres. *J. Power Sources* **2011**, *196*, 1279−1294.

(11) Kishimoto, M.; Lomberg, M.; Ruiz-Trejo, E.; Brandon, N. P. Numerical modeling of nickel-infiltrated gadolinium-doped ceria electrodes reconstructed with focused ion beam tomography. *Electrochim. Acta* **2016**, *190*, 178−185.

(12) Williams, N. J.; Seymour, I. D.; Leah, R. T.; Mukerjee, S.; Selby, M.; Skinner, S. J. Theory of the electrostatic surface potential and intrinsic dipole moments at the mixed ionic electronic conductor (MIEC)−gas interface. *Phys. Chem. Chem. Phys.* **2021**, *23*, 14569−14579.

(13) Williams, N. J.; Seymour, I. D.; Leah, R. T.; Banerjee, A.; Mukerjee, S.; Skinner, S. J. Non-equilibrium thermodynamics of mixed ionic-electronic conductive electrodes and their interfaces: a Ni/CGO study. *J. Mater. Chem. A* **2022**, *10*, 11121−11130.

(14) Chueh, W. C.; Haile, S. M. Electrochemistry of mixed oxygen ion and electron conducting electrodes in solid electrolyte cells. *Annu. Rev. Chem. Biomol. Eng.* **2012**, *3*, 313−341.

(15) Schmid, A.; Fleig, J. The Current-Voltage Characteristics and Partial Pressure Dependence of Defect Controlled Electrochemical Reactions on Mixed Conducting Oxides. *J. Electrochem. Soc.* **2019**, *166*, F831−F846.

(16) Fleig, J.; Jamnik, J. Work Function Changes of Polarized Electrodes on Solid Electrolytes. *J. Electrochem. Soc.* **2005**, *152*, No. E138.

(17) Fleig, J.; Merkle, R.; Maier, J. The p(O2) dependence of oxygen surface coverage and exchange current density of mixed conducting oxide electrodes: Model considerations. *Phys. Chem. Chem. Phys.* **2007**, *9*, 2713−2723.

(18) Guan, Z. Probing and Tuning Far-from-Equilibrium Oxygen Exchange Kinetics on Electrochemical Solid-Gas Interfaces. Ph.D. Thesis, Stanford University, 2018.

(19) Nenning, A.; Opitz, A. K.; Rameshan, C.; Rameshan, R.; Blume, R.; Hävecker, M.; Knop-Gericke, A.; Rupprechter, G.; Klötzer, B.; Fleig, J. Ambient pressure XPS study of mixed conducting perovskite-type SOFC cathode and anode materials under well-defined electrochemical polarization. *J. Phys. Chem. C* **2016**, *120*, 1461−1471.

(20) Hansen, H. A.; Wolverton, C. Kinetics and thermodynamics of H_2O dissociation on reduced CeO_2 (111). *J. Phys. Chem. C* **2014**, *118*, 27402−27414.

(21) Cheng, Z.; Sherman, B. J.; Lo, C. S. Carbon dioxide activation and dissociation on ceria (110): A density functional theory study. *J. Chem. Phys.* **2013**, *138*, 014702.

(22) Kondepudi, D.; Prigogine, I. *Modern Thermodynamics: From Heat Engines to Dissipative Structures*; John Wiley & Sons, 2015.

(23) Chen, L. D.; Urushihara, M.; Chan, K.; Nørskov, J. K. Electric Field Effects in Electrochemical CO_2 Reduction. *ACS Catal.* **2016**, *6*, 7133−7139.

(24) Wang, X. P.; Li, X. B.; Chen, N. K.; Zhao, J. H.; Chen, Q. D.; Sun, H. B. Electric field analyses on monolayer semiconductors: The example of InSe. *Phys. Chem. Chem. Phys.* **2018**, *20*, 6945−6950.

(25) Feng, Z. A.; Gabaly, F. E.; Ye, X.; Shen, Z.-x.; Chueh, W. C. Fast vacancy-mediated oxygen ion incorporation across the ceria−gas electrochemical interface. *Nat. Commun.* **2014**, *5*, 4374.
(26) Wang, Z.; Peng, R.; Zhang, W.; Wu, X.; Xia, C.; Lu, Y. Oxygen reduction and transport on the $La_{1-x}Sr_xCo_{1-y}Fe_yO_{3-\delta}$ cathode in solid oxide fuel cells: A first-principles study. *Journal of Materials Chemistry A* **2013**, *1*, 12932−12940.
(27) Fleig, J. On the current-voltage characteristics of charge transfer reactions at mixed conducting electrodes on solid electrolytes. *Phys. Chem. Chem. Phys.* **2005**, *7*, 2027−2037.
(28) Zhu, M.; Yu, M.; Xia, M.; Li, B.; Yu, P.; Gao, S.; Qi, Z.; Liu, L.; Chen, Y.; Guan, H. VASP: Virtualization assisted security monitor for cross-platform protection. *Proceedings of the ACM Symposium on Applied Computing* **2011**, 554−559.
(29) Blöchl, P. E. Projector augmented-wave method. *Phys. Rev. B* **1994**, *50*, 17953−17979.
(30) Castleton, C. W.; Lee, A.; Kullgren, J. Benchmarking Density Functional Theory Functionals for Polarons in Oxides: Properties of CeO2. *J. Phys. Chem. C* **2019**, *123*, 5164−5175.
(31) Perdew, J. P.; Burke, K.; Ernzerhof, M. Generalized gradient approximation made simple. *Phys. Rev. Lett.* **1996**, *77*, 3865−3868.
(32) Boettcher, S. W.; Oener, S. Z.; Lonergan, M. C.; Surendranath, Y.; Ardo, S.; Brozek, C.; Kempler, P. A. Potentially Confusing: Potentials in Electrochemistry. *ACS Energy Lett.* **2021**, *6*, 261−266.
(33) Dudarev, S. L.; Botton, G. A.; Savrasov, S. Y.; Szotek, Z.; W, M. T.; Sutton, A. P. Electronic Structure and Elastic Properties of Strongly Correlated Metal Oxides from First Principles: LSDA + U, SIC-LSDA and EELS Study of UO2 and NiO. *Physica Status Solidi (A) Applications and Materials Science* **1998**, *166*, 429−443.
(34) Castleton, C.; Kullgren, J.; Hermansson, K. Tuning LDA+ U for electron localization and structure at oxygen vacancies in ceria. *J. Chem. Phys.* **2007**, *127*, 244704.
(35) Grau-Crespo, R.; Corà, F.; Sokol, A. A.; de Leeuw, N. H.; Catlow, C. R. A. Electronic structure and magnetic coupling in $FeSbO_4$: A DFT study using hybrid functionals and GGA + U methods. *Phys. Rev. B* **2006**, *73*, 035116.
(36) Larsen, A. H.; Mortensen, J. J.; Blomqvist, J.; Castelli, I. E.; Christensen, R.; Dułak, M.; Friis, J.; Groves, M. N.; Hammer, B.; Hargus, C.; et al. The atomic simulation environment—a Python library for working with atoms. *J. Phys.: Condens. Matter* **2017**, *29*, 273002.
(37) Youssef, M.; Van Vliet, K. J.; Yildiz, B. Polarizing Oxygen Vacancies in Insulating Metal Oxides under a High Electric Field. *Phys. Rev. Lett.* **2017**, *119*, 126002.
(38) Symington, A. R.; Molinari, M.; Moxon, S.; Flitcroft, J. M.; Sayle, D. C.; Parker, S. C. Strongly Bound Surface Water Affects the Shape Evolution of Cerium Oxide Nanoparticles. *J. Phys. Chem. C* **2020**, *124*, 3577−3588.
(39) Feng, Z. A.; Machala, M. L.; Chueh, W. C. Surface electrochemistry of CO_2 reduction and CO oxidation on Sm-doped CeO_{2-x}: Coupling between Ce^{3+} and carbonate adsorbates. *Phys. Chem. Chem. Phys.* **2015**, *17*, 12273−12281.
(40) Sala, E. M.; Mazzanti, N.; Mogensen, M. B.; Chatzichristodoulou, C. Current understanding of ceria surfaces for CO_2 reduction in SOECs and future prospects − A review. *Solid State Ionics* **2022**, *375*, 115833.

Recommended by ACS

pH Effects in a Model Electrocatalytic Reaction Disentangled
Xinwei Zhu, Michael Eikerling, *et al.*
MARCH 01, 2023
JACS AU
READ

Electron Transport through Nanoconfined Ferrocene Solution: Density Functional Theory—Nonequilibrium Green Function Approach
Ji Il Choi, Seung Soon Jang, *et al.*
JANUARY 27, 2023
THE JOURNAL OF PHYSICAL CHEMISTRY C
READ

Unraveling the Charge Distribution at the Metal-Electrolyte Interface Coupling in Situ Surface Resonant X-Ray Diffraction with Ab Initio Calculations
Yvonne Soldo-Olivier, Yvonne Gründer, *et al.*
FEBRUARY 01, 2022
ACS CATALYSIS
READ

Compressive-Strain-Facilitated Fast Oxygen Migration with Reversible Topotactic Transformation in $La_{0.5}Sr_{0.5}CoO_x$ via All-Solid-State Electrolyte Gating
Zhuo Yin, Baogen Shen, *et al.*
SEPTEMBER 15, 2022
ACS NANO
READ

Get More Suggestions >

https://doi.org/10.1021/acs.nanolett.2c02468
Nano Lett. 2022, 22, 7515−7521